nature catalysis

Article

https://doi.org/10.1038/s41929-025-01342-5

Dissolved Fe species enable a cooperative solid–molecular mechanism for the oxygen evolution reaction on NiFe-based catalysts

Received: 22 December 2023

Accepted: 9 April 2025

Published online: 20 May 2025

Check for updates

Chunguang Kuai[1] ✉, Liping Liu[2,8], Anyang Hu[1,8], Yan Zhang[3], Yuxin Zhang[1], Dawei Xia[1], Dennis Nordlund[3], Dimosthenis Sokaras[3], Donato Decarolis[4], Diego Gianolio[4], Hongliang Xin[2] ✉, Luxi Li[5] ✉ & Feng Lin[1,6,7] ✉

The oxygen evolution reaction is a key process in many energy technologies, but improving its efficiency remains challenging due to the energy scaling relationships that limit the reaction kinetics on conventional single-active-site solid catalysts. Here we report a cooperative solid–molecular mechanism for oxygen evolution on NiFe-based hydroxide electrocatalysts. By identifying the critical interfacial species and understanding their dynamics, we find that molecular FeO_4^{2-} species, derived from the dissolution of Fe from the solid catalyst, act as molecular co-catalysts that participate in the critical O–O bond-formation step along with solid sites. This synergistic mechanism, involving both solid and molecular active species, circumvents the typical scaling limitations observed for solid catalysts alone. Our findings reveal an unconventional solid–molecular mechanism that governs electrocatalysis at the solid–liquid interface and suggest a strategy for transcending scaling constraints through cooperative multi-site catalysis.

The oxygen evolution reaction (OER) on solid catalysts is generally believed to proceed via a four-step process, with each step involving distinct intermediates[1–14]. The kinetics of these steps are restricted by the linear adsorption-energy scaling relationships between these intermediates[15,16]. Reducing the energy barrier for O–O bond formation without compromising the other elementary steps is essential for improving the oxygen evolution activity[17–20]. Designing a solid catalyst structure may bypass this limitation[21–23]. However, owing to the dissolution/redeposition of surface metal cations, the pre-designed structure can be substantially modified during electrocatalysis[2,24–27], making it challenging to break the theoretical scaling relationship solely via structural design of the solid catalyst. Can the dissolved metal cations, which are not geometrically confined to the solid surface, participate in electrocatalytic reactions? Answering this question could provide opportunities for circumventing the usual adsorption-energy scaling limitations.

Dynamic dissolution/redeposition of surface metal cations is ubiquitous in heterogeneous electrocatalysis[28–31]. The discussion on this issue in OER catalysis dates back to Corrigan who, in 1987, investigated the effect of Fe impurities on the OER performance of Ni oxide electrodes[32]. Subsequent studies revealed that even minute traces of Fe in the electrolyte significantly enhance the performance of the Ni oxide electrode[31,33,34]. Nevertheless, the precise role of Fe in the electrolyte remains unknown. Through a detailed investigation of the electrochemical performance when introducing Fe into the electrolyte, Boettcher and colleagues[35] proposed that Fe species can be redeposited

[1]Department of Chemistry, Virginia Tech, Blacksburg, VA, USA. [2]Department of Chemical Engineering, Virginia Tech, Blacksburg, VA, USA. [3]Stanford Synchrotron Radiation Lightsource, SLAC National Accelerator Laboratory, Menlo Park, CA, USA. [4]Diamond Light Source, Harwell Science & Innovation Campus, Didcot, UK. [5]Advanced Photon Source, Argonne National Laboratory, Argonne, IL, USA. [6]Macromolecules Innovation Institute, Virginia Tech, Blacksburg, VA, USA. [7]Department of Materials Science and Engineering, Virginia Tech, Blacksburg, VA, USA. [8]These authors contributed equally: Liping Liu, Anyang Hu. ✉e-mail: cgkuai@outlook.com; hxin@vt.edu; luxili@anl.gov; fenglin@vt.edu

at edge sites of the Ni oxide electrode, functioning as highly reactive solid active sites. Some recent studies have also shown a strong correlation between dissolution/redeposition and the water oxidation activity[24,28,30,36,37]. However, these studies have focused mainly on the solid surface, and the parts played by dissolved metal cations have not been probed directly, resulting in an incomplete understanding of the OER mechanism at the solid–liquid electrochemical interface[38–45].

Here we report a cooperative solid–molecular mechanism for the OER, where molecular species dissolved from the solid surface act as co-catalysts in the rate-determining O–O bond-formation step on benchmark NiFe-based hydroxide electrocatalysts. This mechanism involves a solid Fe catalytic centre and a mobile molecular ferrate(VI) oxyanion (FeO_4^{2-}) co-catalyst in relaying key oxygen intermediates, distinct from the traditional pathways. Such a cooperative solid–molecular catalytic mechanism facilitates the key O–O bond-formation step and enhances the catalytic activity by going beyond the linear scaling constraints observed on monofunctional solid catalysts. These findings offer insights into tuning the solid–electrolyte interface for cooperative catalysis via a solid–molecular mechanism.

Results

Electrode–electrolyte interface dynamics during the OER

We used ultrathin NiFe catalysts as the platform, prepared using a previously developed method[46] (Supplementary Fig. 1). The electrode was prepared via drop casting a catalyst ink onto carbon paper (Supplementary Fig. 2). During the OER, these catalysts undergo dynamic changes both electronically and chemically[29]. We first applied electrochemical quartz crystal microbalance and operando synchrotron X-ray fluorescence microscopy (XFM)[47,48] to investigate the dynamics of metal ions at the solid–liquid interface during electrochemical cycling, with a focus on both the solid and liquid phases. Supplementary Note 1 provides details about these measurements.

The electrode undergoes severe dissolution during the initial rounds of cyclic voltammetry (Supplementary Fig. 3). After dissolution and redeposition had reached a dynamic balance for each cycle, we then studied the dynamic behaviour of the Fe and Ni species during the OER (Fig. 1). There is a clear link between the OER current density and mass change (Fig. 1a and Supplementary Fig. 4). Notably, reversible mass changes are observed during cyclic voltammetry scans (Fig. 1a), with an increase in electrode mass at more positive potentials.

Our focus then turned towards discerning the factors driving the observed mass variation during the OER. Operando XFM results obtained at the electrode shed light on this dynamic mass change, primarily establishing a correlation with Ni and Fe species, as outlined in Supplementary Figs. 5 and 6. The mobile Fe species are defined as Fe species present in the electrolyte, either dissolved from the mixed NiFe hydroxide (MNF) electrode or from the pre-added iron gluconate in this study. Notably, with and without the addition of iron gluconate to the electrolyte, the Ni and Fe species exhibit similar potential-dependent mass-change behaviour during the OER. On the electrode, both Ni and Fe exhibit minimal mass changes at the OER onset potential of 1.43 V versus the reversible hydrogen electrode (RHE) (Supplementary Figs. 5 and 6). As the applied potential is increased, there is a clear mass increase for both Ni and Fe. Conversely, as the potential is brought down to the open-circuit potential (OCP), both Ni and Fe show a decrease in mass. These findings demonstrate the mobile characteristic of Ni and Fe species during the OER.

Our inquiry then extends to the dynamic behaviour of these species at the electrode–electrolyte interface (Fig. 1b–e and Supplementary Figs. 7–16). We observe both Ni and Fe species in the electrolyte even at the OCP (Supplementary Figs. 7–11), which can be attributed to the dynamic dissolution and redeposition of the solid hydroxide catalyst[30,49]. Driven by the difference in chemical potential between the solid electrode and the electrolyte, a clear interfacial region with different chemical structures will be formed[48,50]. A boundary differentiating the electrode and electrolyte becomes apparent in the Ni distribution map, delineating an interfacial diffusion layer that spans around 10 µm into the electrolyte (Fig. 1c and Supplementary Figs. 8 and 9). By correlating the fluorescence intensity of Fe and Ni at the electrode and interface with the current density across various potentials, we observe a positive correlation between the current density and the fluorescence intensity of both Fe and Ni, whether measured on the electrode or in the interfacial region (Fig. 1d,e and Supplementary Fig. 10). As the potential is increased, metal ions dissolved into the bulk electrolyte are driven towards the electrode surface, increasing the metal species both on the electrode and in the interfacial region[6].

Although both Ni and Fe are discernible at the interface, the introduction of additional Ni cations into the electrolyte shows a marginal impact on the OER performance compared with the addition of Fe cations (Supplementary Figs. 17 and 18). It was reported that Ni primarily acts as a host for Fe species[37], thereby enhancing the conductivity and facilitating the formation of high-valent Fe (ref. 6). After introducing Ni into the electrolyte, the adsorption and redeposition of the Ni species will provide more host structures for the Fe species, resulting the slightly enhanced performance. The Fe cations added to the electrolyte introduce a much higher dynamic response than the Ni species (Supplementary Figs. 5 and 6). Therefore, these results show that mobile Fe species play a pivotal role in the OER, which led us to investigate the intricate dynamics of the mobile Fe species.

Dynamics of different Fe species during the OER

Our previous studies showed the gradual transformation of the lattice Fe (that is, $Ni_{0.75}Fe_{0.25}(OH)_2$) into segregated Fe (that is, FeOOH) during the OER[29]. These two species are both in solid form on the electrode during the OER. It has been reported that FeO_4^{2-} species can also be produced at high potentials during the OER[51,52]. Here we use ultraviolet-visible (UV-vis) spectroscopy to detect the presence of FeO_4^{2-} species in our system. As both high pH and Na^+ concentrations can alleviate the decomposition of FeO_4^{2-} species in the solution[53], we used a highly concentrated alkali electrolyte with Na^+ for the measurements. After holding the MNF electrode at 1.63 and 1.73 V vs RHE (Supplementary Figs. 19 and 20 and Fig. 2a,b), clear double peaks at around 505 and 582 nm appeared after long-term chronoamperometry measurements at both potentials, which is an indication that the FeO_4^{2-} species have been formed during the OER[51]. Quantitative analysis for the sample measured at 1.73 V vs RHE based on the standard lines of 505 and 582 nm show comparable values of 1.99 and 1.75 µmol l^{-1}, respectively (Fig. 2b). The above results support the production of FeO_4^{2-} species during the OER.

To further confirm the presence of FeO_4^{2-} species, the operando X-ray absorption spectrum of the sample at 1.63 V vs RHE was compared with those obtained for a K_2FeO_4 solution in 1 M KOH and a solid K_2FeO_4 sample (Fig. 2c). The spectra of the K_2FeO_4 solution and the solid K_2FeO_4 pellet feature two key characteristics: a pronounced pre-edge peak at around 7,114.9 eV and a reduced white line intensity, both of which are indicative of FeO_4^{2-}. However, the pre-edge peak of the K_2FeO_4 solution is weaker than that of pure K_2FeO_4 (ref. 54), indicating partial decomposition. Thus, the reference X-ray absorption spectrum of the K_2FeO_4 solution is a superposition of FeO_4^{2-} and its decomposed FeOOH product. We then compared the R-space of the extended X-ray absorption fine-structure (EXAFS) spectra (Fig. 2d). Two obvious Fe–O peaks can be seen at around 1.05 and 1.44 Å, which can be ascribed to the Fe–O bond in FeO_4^{2-} (~1.66 Å) and FeOOH (~2.10 Å), respectively. The peak at ~1.05 Å is also evident for our MNF sample when measured at 1.63 V vs RHE (Fig. 2d), which is clear evidence that FeO_4^{2-} species were present during the OER. The EXAFS fitting reveals that the ultrashort bond length is around 1.65 Å (Supplementary Figs. 21 and 22 and Supplementary Table 2), which matches well with the Fe–O bond length in FeO_4^{2-} (ref. 54).

https://doi.org/10.1038/s41929-025-01342-5

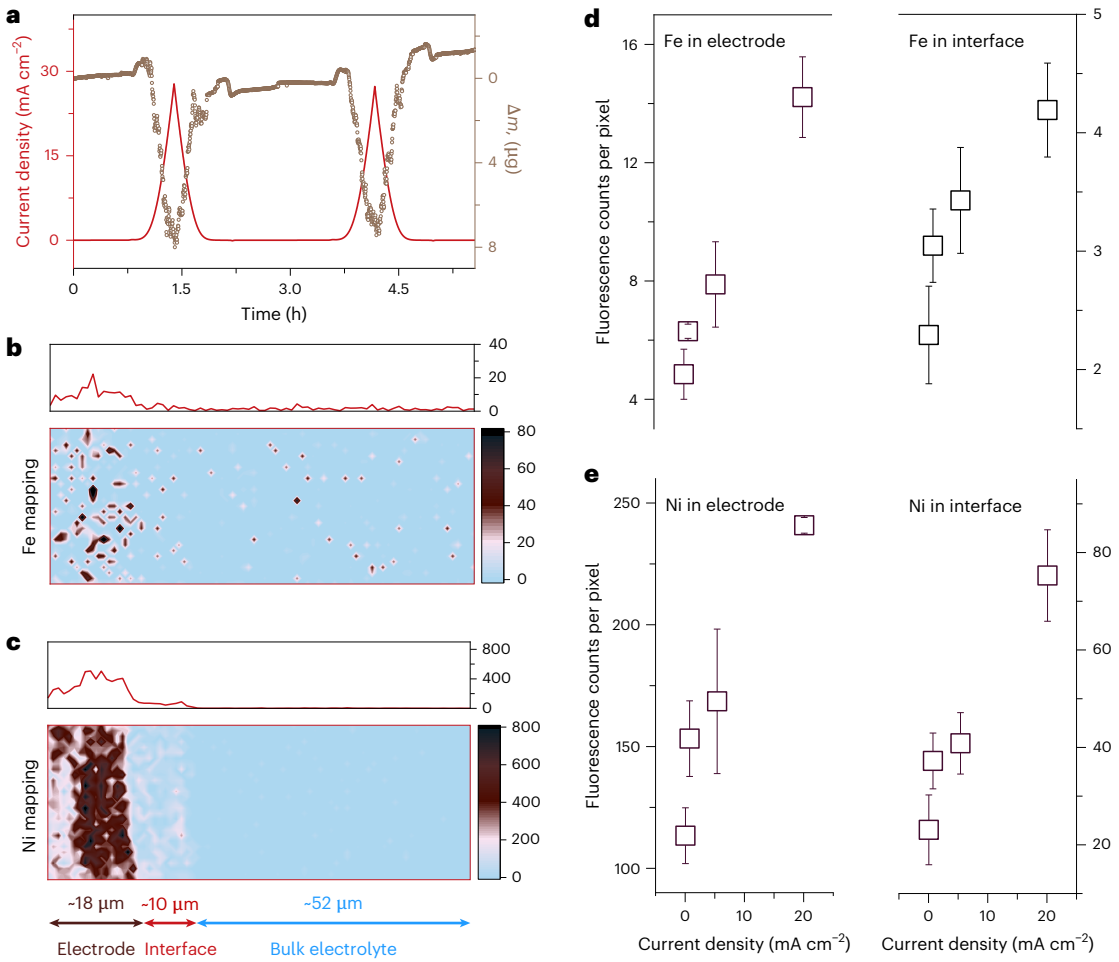

Fig. 1 | Dynamic behaviour at the electrode–electrolyte interface. a, Cyclic voltammetry cycles and mass variations of the MNF electrode following the initial five cyclic voltammetry cycles when dissolution/redeposition reaches a dynamic equilibrium. The mass variation (Δm) is monitored during cyclic voltammetry scans between 1.13 and 1.63 V versus RHE, at a scan rate of 1 mV s^{-1}. **b**,**c**, Operando XFM images showing the fluorescence intensity distribution of Fe (**b**) and Ni (**c**) ions from the electrode to the electrolyte at 1.63 V versus RHE. The curve above each XFM image shows the fluorescence intensity distribution from the electrode to the electrolyte. The colour scale indicates the fluorescence intensity, which is determined by the element concentration, X-ray fluorescence yields, mass attenuation coefficient and X-ray penetration of the incident and reflection beam in the electrolyte. These factors collectively result in the huge difference in signal magnitude for Ni and Fe. However, when considering Ni and Fe separately, the intensities are in a positive relationship with the concentration of the metal ions. The length scale of the fluorescence intensity distribution is the same for both metals. The spatial resolution is 1 × 1 μm for each. The units for the fluorescence intensity are fluorescence counts per pixel. **d**,**e**, Fluorescence intensity versus the OER current density at various potentials for Fe (**d**) and Ni (**e**). The electrode and interface regions, as shown in **c**, are considered separately. The data points shown represent the average intensity of the entire region. The error bars denote the s.d. of six consecutive XFM scans. Data are presented as mean ± s.d. From left to right, the applied potentials for the data are 1.43, 1.48, 1.53 and 1.63 V vs RHE.

We used operando hard X-ray absorption spectroscopy (hXAS) to investigate the dynamic electronic behaviour of Fe species during the OER. Here we first discuss the hXAS measurements for the electrode. At 1.53 V vs RHE, both Fe and Ni swiftly converge towards their equilibrium oxidation states, as shown in Supplementary Fig. 23. By lowering the overpotential all the way down to the onset of the OER (1.43 V vs RHE), we can spectroscopically probe intermediate species under intrinsic kinetic control. A noteworthy observation is the oscillation in the oxidation state of Fe at the OER onset potential (Supplementary Figs. 24 and 25). Supplementary Figure 24 shows the Fe K-edge XAS spectrum at the OER onset potential (1.43 V vs RHE), displaying oxidation-state oscillations that can be fitted on the basis of the Fe spectrum at 1.63 V vs RHE and the spectrum at the OCP (Supplementary Fig. 25). The ratio of these components shows oscillatory behaviour with the measurement sequence (Supplementary Fig. 25h). By contrast, the Ni species show a continuous rise in the oxidation state (Supplementary Fig. 26). We carried out a further analysis on the EXAFS data of both Fe and Ni obtained at this potential (Supplementary Fig. 27). During the first measurement, the local structure changed dramatically both for Ni and Fe, especially at the first shell, which represents the Fe–O bond structure. This result indicates that substantial structural rearrangement occurs during the initial stage of catalyst oxidation. After three consecutive measurements, the Ni oxide host structure approached its stabilized high-oxidation structure obtained at 1.63 V vs RHE. Meanwhile, for Fe, during seven consecutive measurements, the Fe–O bond structure changed dynamically. As this potential is around the OER onset, these dynamic changes could be related to the OER process, and the high-oxidation-state Fe generated may not be stable. The above observation suggests that there are dynamic structural and electronic changes in the Fe centres during the OER.

Relative to the Ni centre, the Fe local structure demonstrates more pronounced dynamic alterations at OER potentials, especially beyond the second scattering shell (Fig. 2e and Supplementary Fig. 28). These pronounced dynamic alterations may be related to the transformation among different Fe species during the OER. In the following, we use the X-ray spectroscopy results to explore the dynamic changes in the Fe

https://doi.org/10.1038/s41929-025-01342-5

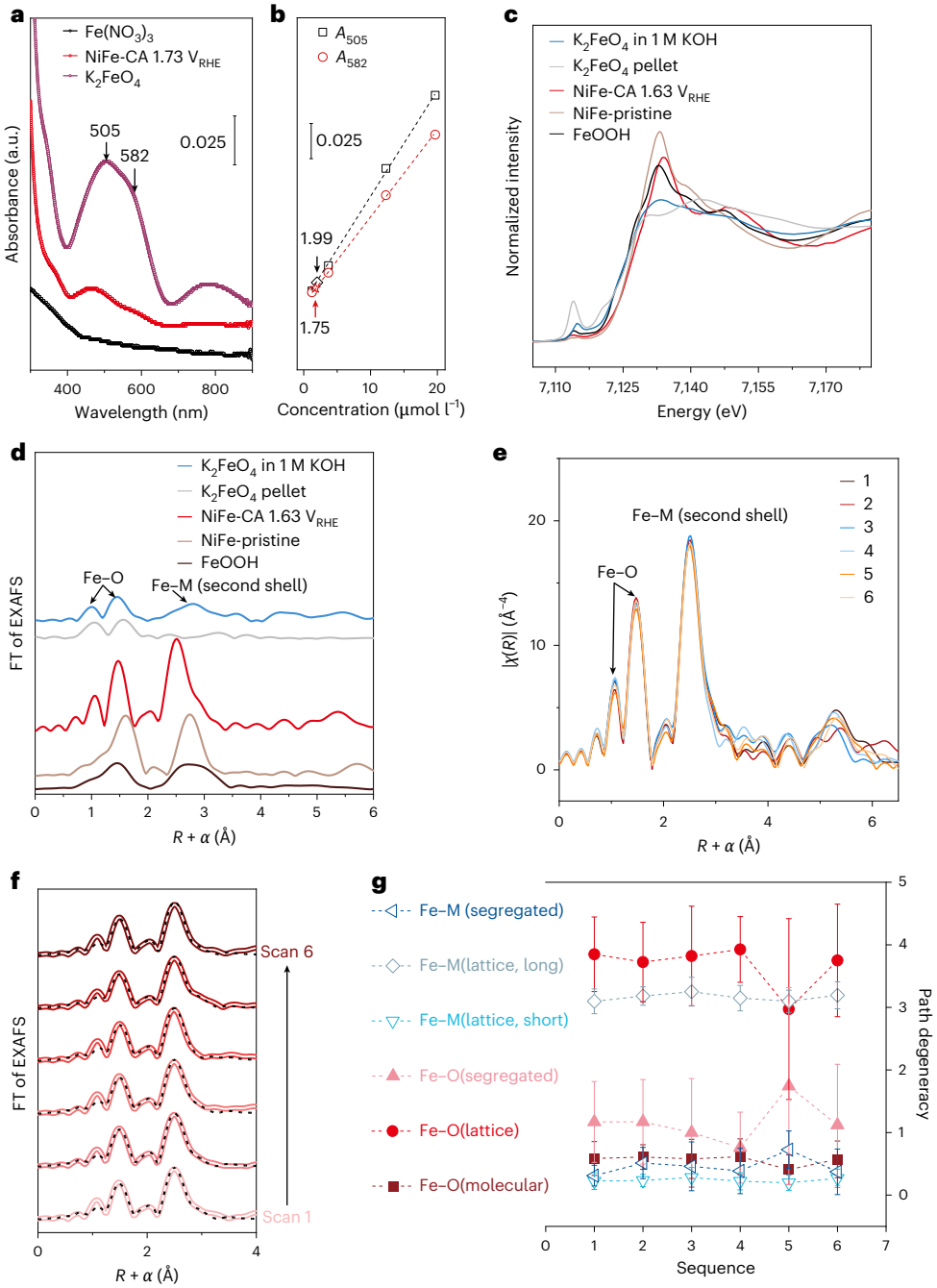

Fig. 2 | Dynamic local structural change in Fe species during the OER. **a**, Identification of FeO_4^{2-} ions in the electrolyte after electrochemical measurement. Purple: standard UV-vis spectrum of K_2FeO_4 in 5 M NaOH + 5 M KOH. Red: UV-vis spectrum of the electrolyte after a 3.5 h chronoamperometry (CA) measurement at 1.73 V vs RHE in 5 M NaOH + 5 M KOH. Black: standard UV-vis spectrum of $Fe(NO_3)_3$ solution. **b**, Quantification of the FeO_4^{2-} species in the electrolyte after the chronoamperometry measurement. After dissolving K_2FeO_4 powder in 5 M KOH + 5 M NaOH solution, where FeO_4^{2-} can be stabilized, the concentration of Fe in the solution was determined via microwave plasma atomic emission spectroscopy measurements. Standard linear relationships were established between the absorbance (A) intensities and the concentrations. Following the chronoamperometry measurement, the FeO_4^{2-} concentration in the NiFe sample's electrolyte is assessed using the established linear relationships. This yields comparable values of 1.99 and 1.75 μmol l^{-1} at the 505 and 582 nm lines, respectively. The blue diamond and red star symbol represent the absorption of the NiFe sample's electrolyte at 505 and 582 nm. **c**, Fe K-edge X-ray absorption near-edge spectroscopy measurements of the reference samples and NiFe samples in different states. **d**, Fe K-edge EXAFS measurements of reference samples and the NiFe samples in different states. Two K_2FeO_4 reference samples were measured: one is in liquid form and the other is in solid form. The liquid sample is prepared by dissolving 0.1 M K_2FeO_4 in 1 M KOH. K_2FeO_4 powder (100 mg) is quickly pressed to form the solid pellet in air, and is then sealed using Kapton tape. Note that we still can see the Fe–O peak around 1.5 Å in the solid K_2FeO_4 pellet, indicating partial decomposition still occurs even for the sealed sample in the solid state. **e**, Dynamic local structural behaviour of Fe species at 1.53 V vs RHE, where six consecutive scans were taken at this potential. **f**, EXAFS fitting of Fe at 1.53 V vs RHE. The solid lines represent the k^3-weighted Fourier transformed scattering amplitude of the Fe K-edge EXAFS spectra. The dashed lines represent the fitting results. FT, Fourier transform. **g**, Dynamic evolution of the scattering paths for the sample measured at 1.53 V vs RHE. The sequence refers to measurement sequence of the six consecutive scans in **e**. Data presented by open and filled symbols indicate the Fe–M and Fe–O path degeneracies in different local structures, respectively. The error bars represent the fitting error.

local structure during the OER (Fig. 2f,g, Supplementary Fig. 21, Supplementary Table 3 and Supplementary Note 2). Our current results confirm that there are at least three Fe species during the OER, which are molecular FeO_4^{2-}, lattice Fe and segregated Fe. Here, we investigate the dynamic changes in these three distinct Fe species at 1.53 V vs RHE (Fig. 2f,g). The outcomes portray the dynamic interplay between segregated Fe, lattice Fe and molecular FeO_4^{2-}. The degeneracy of the paths associated with molecular FeO_4^{2-} and lattice Fe shows a positive correlation. By contrast, the characteristics shown by segregated Fe delineate a trajectory reverse to those of lattice Fe and molecular FeO_4^{2-}.

In summary, our operando structural analyses confirm that there is dynamic evolution between several Fe species during the OER, that is, lattice Fe, segregated Fe and molecular FeO_4^{2-}. They dynamically evolve, both electronically and chemically, during the oxygen release.

O–O bond formation promoted by the molecular Fe species

Our investigation now turns to understanding the functional implications of molecular Fe species, achieved through the manipulation of their properties and subsequent assessment of the resultant changes in OER performance. Supplementary Figure 29 shows our strategy of using light illumination in the electrode–electrolyte interfacial region to manipulate the properties of molecular Fe species. On subjecting the electrolyte to light illumination, the molecular Fe species become excited at the interfacial region, yielding a discernible elevation in the OER current density (Fig. 3a). This result further pinpoints the critical role of interfacial molecular Fe on the OER performance. We hypothesize that the excited molecular Fe species increase the OER activity because the O anions in the molecular Fe species participate in the O–O bond-formation process.

To shed light on this hypothesis, we first investigated the oxygen electronic state of the solid MNF catalyst before and after the OER. Obvious O 2*p* holes are identified using O K-edge XAS (indicated by the broad pre-edge peak in the range of 527–530 eV) after the OER, which correspond to 2*p* electron-deficient oxygen sites (μ_1-O at 528.5 eV and μ_2-O at 529 eV) on the catalyst surface[3,55,56] (Fig. 3b). At the OER active potential (1.63 V vs RHE), the relative peak intensity at 528.5 eV decreases compared with 1.43 V vs RHE, where negligible OER occurs (Fig. 3c). After O–O bond formation, oxygen is quickly released, consuming the *O adsorbate at the catalyst surface and resulting in a decrease in the peak intensity at 1.63 V vs RHE. When introducing Fe into the Ni catalyst, the peak at 528.5 eV shows a further decrease at both 1.43 and 1.63 V vs RHE, indicating that O–O bond formation is greatly promoted by the mobile Fe species (Fig. 3b,c). Other than the 2*p* electron-deficient oxygen sites, we also identify another oxygen site located at 530.7 eV, which can be assigned to μ_1-OH (refs. 3,55,56). The accumulated μ_1-OH sites on the catalyst indicate that deprotonation of the μ_1-OH species is thermodynamically unfavourable. At the OER active potential (1.63 V vs RHE), the relative peak intensity at 530.7 eV decreases compared with 1.43 V vs RHE, where negligible OER occurs. As deprotonation becomes favourable at elevated potential, the μ_1-OH species is consumed on the catalyst surface, resulting in a decrease in the peak intensity. Following deprotonation of the μ_1-OH species, an energetically less favourable step involving the formation of an O–O bond will occur[1,18], through coupling between the surface μ_1-O and OH^- in the electrolyte (that is, the adsorbate evolution mechanism (AEM)) or between the surface μ_1-O and the molecular Fe species in electrolyte (that is, the solid–molecular mechanism (SMM)).

To further understand the interaction between the electrode and the molecular Fe species, we also investigated the electronic structure change of the molecular Fe species near the electrode during the OER using operando high-energy-resolution fluorescence-detection X-ray absorption spectroscopy (HERFD-XAS) (Fig. 3d,e and Supplementary Fig. 30). The intensities after the edge jump can reflect the Fe concentration near the electrode[11]. We then use these intensities to normalize the pre-edge peak. Under the OER conditions, the normalized intensity of the pre-edge peak for the MNF interface is higher than that of Fe^{3+} in the bulk electrolyte at the OCP, which confirms that the average oxidation state of the mobile Fe species near the MNF electrode under the OER conditions is higher than 3+ (Fig. 3e). The normalized intensity also increased slightly with a higher applied potential. The enhancement in pre-edge peak intensity provides further evidence of FeO_4^{2-} formation[51,52,57]. However, it is far below the intensity of FeO_4^{2-}, where Fe is in the hexavalent state. We speculate that the kinetics of the interaction between the mobile FeO_4^{2-} species and the O species on the MNF electrode are very high, thus making the average oxidation state of the mobile Fe species near the MNF electrode lower than 6+. To test this hypothesis, we compared the interface of the OER inert carbon fibre at 1.83 V vs RHE with that of the MNF interface. The pre-edge peak is greatly enhanced at the same potential. Its intensity is comparable to that of the pre-edge peak for FeO_4^{2-}, indicating that most of the mobile Fe species at the carbon fibre interface are in the hexavalent state[54]. We also exclude the possibility that the generation of more FeO_4^{2-} on the carbon fibre surface results from a catalytic effect of carbon (Supplementary Fig. 31). The above results show that the interaction between the electrode and the mobile FeO_4^{2-} species is crucial for the OER performance—this is further supported through UV-vis measurements comparing the decomposition rate of FeO_4^{2-} species with and without the NiFe electrode (Supplementary Fig. 32).

Solid–molecular active-centre mechanism

In $Ni(OH)_2$ catalysts, the OER typically follows the lattice oxygen mechanism[58,59]. This mechanism entails a critical step involving the formation of *OOH species adsorbed on 2Ni bridge sites (Supplementary Figs. 33 and 34), which presents an energy barrier of 0.51 eV (Supplementary Fig. 34) at 1.23 V vs RHE. The introduction of 3*d* metal cations, especially Fe, into these catalysts consistently yields an observable enhancement in performance[46]. Under the OER operating conditions, defect-containing MNF and segregated FeOOH catalysts can evolve from the pristine MNF catalysts. To identify the active sites of MNF catalysts for the OER, systematic grand-canonical density functional theory (GC-DFT) calculations were performed to evaluate the OER energetics across various sites and catalysts, in addition to their counterparts with diverse defect types, as detailed in Fig. 4a, Supplementary Figs. 35–37, and Supplementary Notes 4 and 5. Theoretical results show that the Fe top sites of Fe-doped γ-NiOOH and γ-$Fe_{0.25}Ni_{0.75}OOH$ exhibit the highest activity for the OER, with the O–O bond formation as the potential-limiting step and an overpotential (η) of 0.37 and 0.42 V, respectively. They are comparable to literature values[35] after considering the DFT uncertainties[60], and in agreement with the experimental results (Fig. 4a and Supplementary Note 3). Such catalytic OER activity trends are further demonstrated by the well-established linear scaling relation and volcano plot (Fig. 4a,d). These mechanisms involve the evolution of adsorbed O species (*OH, *O and *OOH), which impose a performance limit due to the linear scaling relationship[42] (Fig. 4d). Our experimental results reveal an important aspect of the OER process involving molecular FeO_4^{2-} species. These adsorbed molecular FeO_4^{2-} species emerge as pivotal intermediates, which catalytically facilitate O–O bond formation through interactions with adsorbed O species on the solid electrode.

To further understand the interaction between the molecular FeO_4^{2-} species and the adsorbed O species on the solid electrode, we conducted GC-DFT calculations with hybrid solvation. After identifying the active centre and most abundant surface intermediates (MASI) on the MNF catalysts at different potentials (Fig. 4a,c, Supplementary Fig. 42 and Supplementary Notes 4 and 8), we assessed the thermodynamics of the interaction between *O and the molecular FeO_4^{2-} species, which generates the $*OOFeO_3$ intermediate in step 3′ (Fig. 4b,c). The formation of $*OOFeO_3$ in step 3′ transfers two electrons to the surface in the elementary step and is more thermodynamically favourable than the formation of *OOH in step 3, especially at high potentials (Fig. 4c).

https://doi.org/10.1038/s41929-025-01342-5

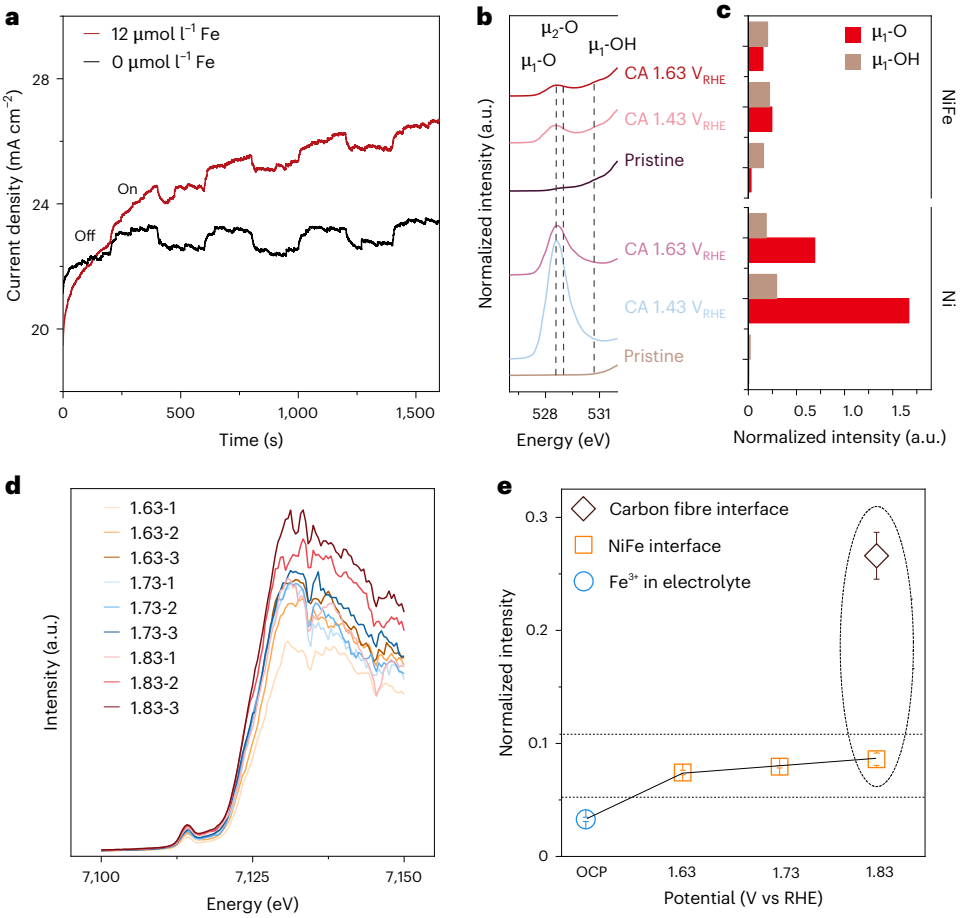

Fig. 3 | Interaction between the electrode and the molecular Fe species. **a**, Influence of light-activated molecular Fe species on the OER performance at 1.63 V vs RHE. **b**, Surface-sensitive O K-edge XAS measurement of the Ni electrode (bottom trio of peaks) and MNF electrode (top trio) before the OER and at different OER potentials in total electron yield mode. The samples were prepared by immediately drying and sealing in an argon-filled bag after the electrochemical measurements to avoid exposure to moisture in the air and to preserve the structural characteristics. **c**, Normalized μ_1-O (528.5 eV) and μ_1-OH (530.7 eV) intensity values of the Ni and MNF electrodes under the conditions shown in **b** in total electron yield mode. **d**, Operando HERFD-XAS spectra of the interfacial area near the MNF electrode at different OER potentials. The measurement point is 8 μm from the electrode surface in the electrolyte with the X-ray direction parallel to the electrode surface. In these experiments, we added iron gluconate to the electrolyte for a concentration of 1 mmol l^{-1}. The potentials applied to the electrode are 1.63, 1.73 and 1.83 V vs RHE. At each potential, three consecutive measurements are taken. **e**, Normalized intensity of the HERFD-XAS pre-edge peaks at 7,114 eV from **d**. The peak intensities are normalized by the intensity of the HERFD-XAS signal after the edge jump at 7,131 eV to eliminate the concentration effect[11]. Each point represents the average peak intensity of three independent scans (detailed spectra are also presented in Supplementary Fig. 30). The error bars are the s.d. values calculated from the three peak intensity data of different measurements, and the data are presented as the mean ± s.d.

Notably, the preference of the SMM over the AEM and the lattice oxygen mechanism at elevated potentials is consistently observed across all investigated sites and catalysts (Supplementary Fig. 37). Further comparison of the formation of *OOH and *$OOFeO_3$ intermediates suggests that the SMM offers a potential pathway to break the linear scaling in conventional OER mechanisms (Fig. 4d). These findings highlight both the critical role and the broad applicability of the SMM in promoting O–O bond formation and enhancing the OER kinetics (Fig. 4c and Supplementary Fig. 37). The methodology for calculating the Gibbs free energy of *$OOFeO_3$ formation is elaborated in Supplementary Fig. 38 and Supplementary Note 6. To complete the catalytic cycle, *$OOFeO_3$ can react with two OH^- (step 4′) via an exergonic process, which releases a gas-phase O_2 and renews both the FeO_4^{2-} anions and the catalysts. Given that step 3′ is a two-electron transfer step, it is likely that the OER rate via the SMM is limited by this step.

Drawing on our experimental and theoretical insights, we introduce a solid–molecular dual-active-centre mechanism for the OER that encompasses both solid and molecular catalytic centres (Fig. 4e). In contrast to the AEM, this mechanism involves a chemical interplay between the molecular Fe species and the *O adsorbate on the solid electrode, facilitating O–O bond formation. This dual-active-site mechanism unfolds through two distinct processes: first, a heterogeneous process involving electrode oxidation and charge transfer between the solid active centres and the adsorbed oxy-intermediates; then, a molecular-assisted process that facilitates O–O bond formation and O_2 release. Manipulation of the electron-hole state either in the molecular Fe or on the electrode surface could subsequently influence the OER performance.

Microkinetic analysis

The proposed mechanism suggests that the Fe concentration in the electrolyte has a direct effect on the OER current density. As depicted in Fig. 5a, our investigation reveals a compelling positive correlation between the OER performance and the concentration of iron gluconate pre-added to the electrolyte. Up to approximately 1.53 V vs RHE, the Tafel slope remains constant at 36 mV dec^{-1}, irrespective of the concentration of iron gluconate. However, above this threshold, the Tafel slope exhibits a notable dependency on the concentration, decreasing from

https://doi.org/10.1038/s41929-025-01342-5

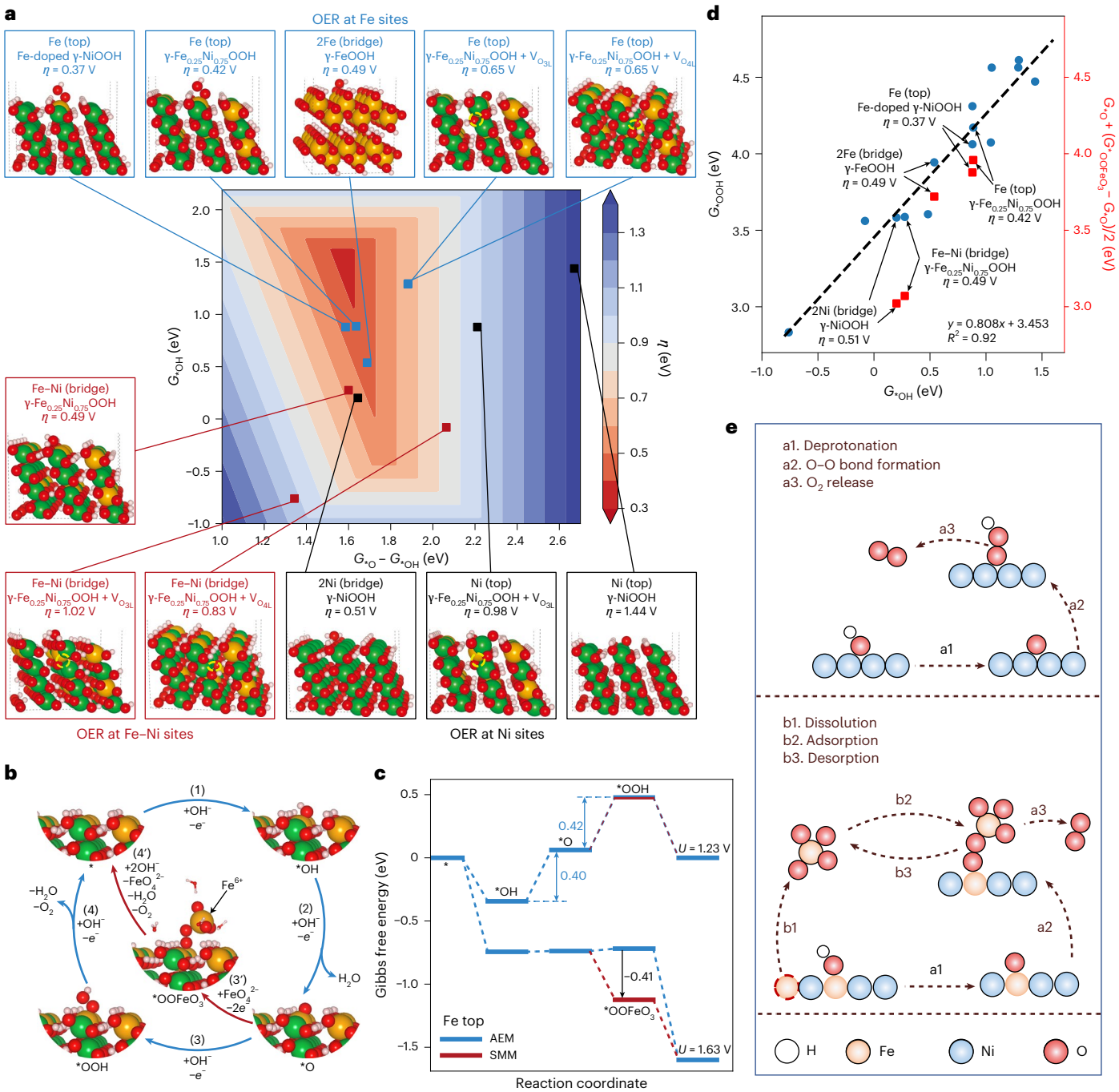

Fig. 4 | Mechanistic understanding and schematic illustration of the SMM. **a**, Theoretical OER overpotentials of various sites and catalysts via the conventional mechanisms, along with an activity volcano plot as a function of $G_{*O} - G_{*OH}$ and G_{*OH}. The computed overpotentials for the OER using GC-DFT are displayed above each structure. All corresponding structures are illustrated with the intermediates, the formation of which is the potential-limiting step. $V_{O_{nL}}$, oxygen vacancy in the *n*th layer. **b**, Proposed OER mechanisms on the Fe top site of γ-$Fe_{0.25}Ni_{0.75}OOH$, representing the MNF catalysts. The outer cycle with blue arrows is the traditional OER pathway via the AEM, whereas the inner step with red arrows proceeds via the SMM. The reference state is FeO_4^{2-} anions at 6 μmol l^{-1}. e^-, electron. **c**, Gibbs free energy (G) of each elementary step in the AEM and SMM. Compared with *OOH formation, the formation of $*OOFeO_3$ is more thermodynamically favourable, notably at higher potentials, suggesting that the SMM is the dominant OER pathway at high applied potentials (U). **d**, Linear energy scaling relationship among diverse sites and catalysts, and comparison between conventional OER mechanisms and the SMM in O–O formation. As the formation of the $*OOFeO_3$ species from *O and molecular FeO_4^{2-} requires the discharge of two electrons, we divided the energetics of the formation of $*OOFeO_3$ species by two and calculate $G_{*O} + (G_{*OOFeO_3} - G_{*O})/2$ to enable the comparison between the formation of *OOH and $*OOFeO_3$ from the same *O intermediate. The results show that $G_{*O} + (G_{*OOFeO_3} - G_{*O})/2$ clearly show a systematic downward from G_{*OOH}, deviating the scaling relation between G_{*OOH} and G_{*OH}. The filled blue circles represent the relationship between G_{*OOH} and G_{*OH}, whereas the filled red squares represent the relationship between $G_{*O} + (G_{*OOFeO_3} - G_{*O})/2$ and G_{*OH}. The dashed line represent the linear fitting result of the filled blue circles data. R^2, the coefficient of determination. **e**, Traditional AEM (top) and the proposed SMM (bottom).

https://doi.org/10.1038/s41929-025-01342-5

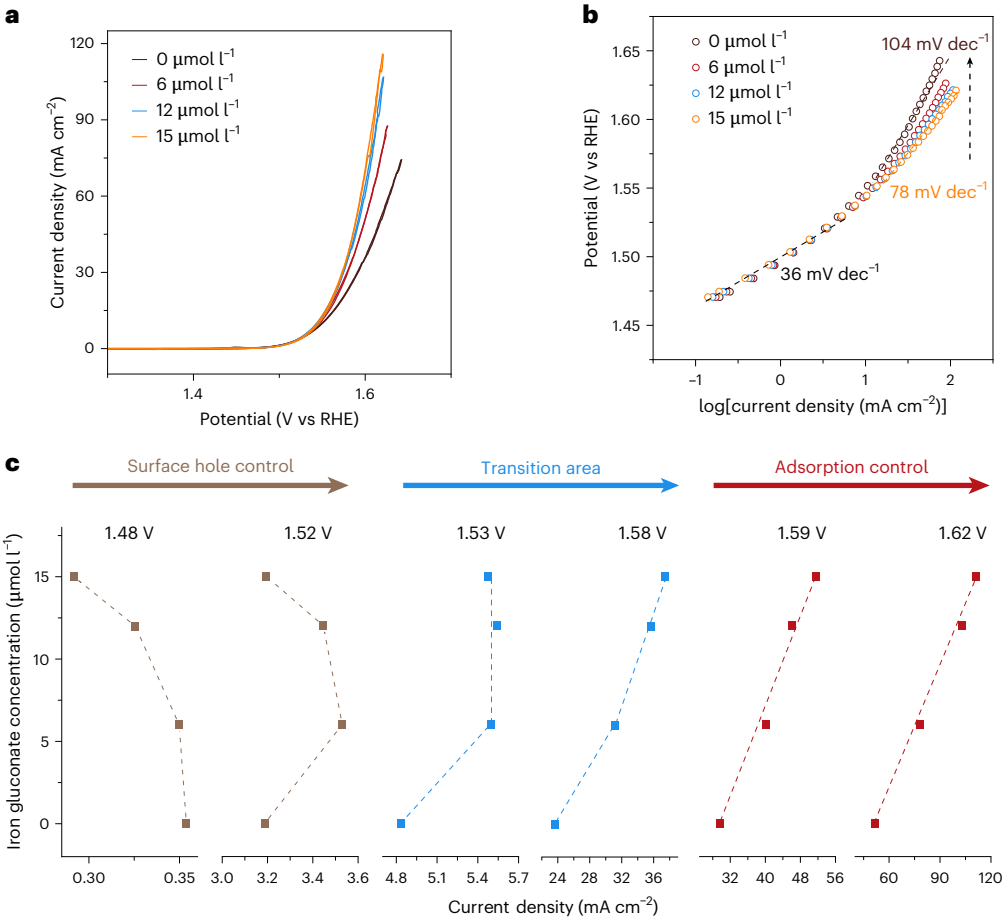

Fig. 5 | OER performance of the MNF catalysts with and without the addition of iron gluconate to the electrolyte. a, Cyclic voltammetry measurements of the MNF catalyst when varying the iron gluconate concentration in the electrolyte. The scan rate is 10 mV s^{-1}. **b**, Tafel plots of the MNF catalyst with different iron gluconate concentrations in the electrolyte. **c**, Relationships between the iron gluconate concentration and OER current density at different potentials.

108 to 78 mV dec^{-1} as the concentration is increased from 0 to 15 μmol l^{-1} (Fig. 5b). The analysis of electrochemical impedance spectroscopy data shows that the OER kinetics shift from charge-transfer control to adsorption control above 1.53 V, due to the adsorption of molecular Fe species (Supplementary Figs. 39–41 and Supplementary Note 7).

These findings highlight the significant contribution of molecular Fe species in NiFe-based electrocatalysts during the OER. Consequently, an in-depth exploration of the kinetic factors that influence the change in the Tafel slope could provide insights into the function of these molecular Fe species. Previous research has associated the transition of the Tafel slope with potential-dependent variations in the surface hole coverage and concentration shifts[3]. When comparing our results with these findings, we conjecture that the adsorbed molecular Fe species may potentially serve as carriers of holes during the OER. Plausibly, the adsorption-controlled process involves a synergistic chemical and electrochemical process, where these hole carriers interact with the adsorbed oxy-intermediate on the electrode.

To gain more insight into the OER kinetics, we performed microkinetic analysis on the basis of our proposed mechanism. Considering that steps 3′ and 3 are the rate-determining steps and proceed in parallel (Fig. 4b), the total current density of the OER can be written as a summation of the current densities from both the AEM and SMM, as shown in the microkinetic modelling of Supplementary Note 8. The microkinetic model indicates that the current density at a specific potential is influenced by two factors: the surface electron-hole coverage and the concentration of molecular FeO_4^{2-}. At low potentials (below 1.53 V vs RHE), the current density is primarily governed by the potential-dependent coverage of surface *O with electron holes, as depicted in Fig. 5b and explained in the Supplementary Note 4. When Fe is introduced, it hinders the oxidation of the Ni centre, resulting in a decrease in surface hole coverage[30,31]. Consequently, this has a slightly negative impact on the current density (Fig. 5c). On surpassing 1.53 V vs RHE, the MASI are identified as *O with an electron hole in it (Fig. 4c and Supplementary Notes 4 and 8). At this point, the adsorption of molecular FeO_4^{2-} starts to dominate the control of the current density (Fig. 5b). This establishes a transitional region between 1.53 and 1.58 V vs RHE, where both the hole coverage and FeO_4^{2-} concentration play crucial roles in determining the current density (Fig. 5c). As the potential continues to rise, the current density becomes solely reliant on the adsorption of molecular FeO_4^{2-} (step 3′). As a consequence, it exhibits a linear relationship with the concentration of Fe^{3+} in the electrolyte (Fig. 5c). Under such high potentials (>1.53 V vs RHE), as step 3′ involves two-electron transfer, the microkinetic model shows that the Tafel slope of the MNF catalysts in the presence of the molecular FeO_4^{2-} species is lower than that of the pristine MNF catalysts, and decreases towards 69 mV dec^{-1} (Supplementary Figs. 42 and 43) with an increasing concentration of molecular FeO_4^{2-} species, aligning well with the experimental observation (Fig. 5b).

Conclusions and discussion

Explaining the critical role of molecular Fe species in the OER, as presented in this study, offers valuable mechanistic insights into the well-documented phenomena of metal dissolution and redeposition at the OER interface. Our findings demonstrate that these molecular

Fe species act as molecular co-catalysts, facilitating crucial O–O bond formation at the solid catalytic centre. By elucidating the pivotal role of dynamic metal redeposition in modulating the reactivity, these findings provide key insights into interfacial processes during oxygen evolution. In contrast to the limitations imposed by the linear adsorption-energy relationship and rigid geometric constraints in traditional solid active-centre mechanisms, this solid–molecular active-centre mechanism introduces a higher degree of freedom for optimizing the OER performance. Owing to the significant structural differences between solid-phase and molecular catalysts, they can complement each other in controlling the OER intermediates. Specifically, in terms of the electronic structure, solid-phase catalysts form band structures with delocalized electronic states, whereas molecular catalysts form molecular orbitals, resulting in localized electronic levels. These differences in electronic structure lead to distinct electron-transfer behaviours between active centres and adsorbed oxygen species, influencing the kinetics of intermediate species. In addition, external factors influence solid-phase and molecular catalysts differently. Solid-phase catalysts expose only their surface to the electrolyte, with their intrinsic properties largely unaffected by the external environment. By contrast, molecular catalysts are fully immersed in the electrolyte, making their chemical and electronic structures highly tunable via the reaction environment. This distinction suggests that a hybrid solid–molecular catalytic system could independently regulate OER intermediates, achieving the synchronized optimization of critical reaction steps. We anticipate that this proposed solid–molecular mechanism will not only advance our understanding of the OER process but also provide opportunities in the design of innovative OER catalytic systems. By integrating both solid and molecular active centres, this approach could help push the OER performance towards the thermodynamic limit, overcoming existing energy scaling constraints and enabling more efficient water-splitting technologies.

Methods

Synthesis of the ultrathin MNF catalysts

First, the metal source (nickel acetate tetrahydrate and ferrous chloride; 0.5 mmol) was dissolved in ethanol (200 ml) and heated to 90 °C, then ammonia (2 ml) was added dropwise to the solution with vigorous stirring. After that, deionized water (100 ml) was added into the mixture. This mixture was then held at 90 °C for 1.5 h under vigorous stirring. After cooling to room temperature, the product was collected through vacuum filtration and re-dispersed into water. After being sonicated for 30 min, the mixture was filtered again through vacuum filtration. The sonication and cleaning steps were repeated at least three times, and the product was collected and dispersed in deionized water (30 ml) for further use.

Preparation of MNF electrode on carbon paper

First, the catalyst (~35 mg) was dispersed in deionized water (30 ml) and sonicated in solution to give a clear yellowish ink. Then, this yellowish ink (0.5 ml) was mixed with methanol (0.5 ml). The mixture was sonicated for 30 min to yield a homogeneously dispersed catalyst ink. Then, the catalyst ink (20 µl) was drop cast onto carbon paper (0.5 × 0.4 cm; Toray Carbon Paper 090, Fuel Cell Store) and dried in air. Subsequently, the electrode was dried further using a vacuum oven at 120 °C for 6 h. The mass loading of the catalysts was around 0.06 mg cm^{-2}, as calculated from the concentration and volume of the catalyst ink cast onto the carbon paper.

Preparation of MNF electrode on Au electrode

First, the catalyst (~35 mg) was dispersed in deionized water (30 ml) and sonicated in solution to give a clear yellowish ink. Then, this yellowish ink (0.5 ml) was mixed with methanol (0.5 ml) and Nafion solution (20 µl). The mixture was sonicated for 30 min to yield a homogeneously dispersed catalyst ink. Then, the catalyst ink (20 µl) was drop cast onto a 5-mm-diameter Au electrode and dried in air. Subsequently, the electrode was dried further using a vacuum oven at 120 °C for 6 h. The mass loading of the catalysts was around 0.06 mg cm^{-2}, as calculated from the concentration and volume of the catalyst ink cast on the Au electrode.

OER measurements

Electrochemical measurements were carried out using a CHI 760E potentiostat and a BioLogic SP-150 potentiostat. For the electrochemical measurements, a three-electrode configuration was used with a graphite carbon rod as the counter electrode and Hg/HgO as the reference electrode. The applied potential was converted to the RHE scale using the following equation:

$$E(\mathrm{RHE}) = E(\mathrm{Hg/HgO}) + 0.059\mathrm{pH} + 0.098 \quad (1)$$

where E represents the applied potential on the working electrode. The electrolyte used here is 1 M KOH with the addition of iron gluconate at different concentrations. For the electrolyte without adding iron gluconate, we performed an Fe purification procedure before use according to the method in ref. 6. To precisely control the amount of Fe added to the solution, we used iron gluconate as the Fe source, as gluconate can act as an effective chelating agent in alkaline environments.

Synchrotron XFM measurements

Samples for operando synchrotron XFM analysis were prepared with the same method as used for the electrochemical measurements. XFM measurements were conducted at the 2-ID-D and 2-ID-E beamlines of Advanced Photon Source, Argonne National Laboratory. The samples were raster-scanned using a submicrometre focused 10 keV X-ray beam with a step size of 1 µm. The fluorescent X-rays were detected using an energy-dispersive Vortex silicon drift detector. The schematic of the experimental set-up can be found in refs. 47,48. The raw data were processed and quantified using XRF-MAPS software[61].

Synchrotron XAS measurements

The XAS measurements were carried out at Stanford Synchrotron Radiation Lightsource, SLAC National Accelerator Laboratory, except for the K_2FeO_4 standards, which were measured at Diamond Light Source. For all of the experiments, samples were prepared on carbon paper (Toray Carbon Paper 090) in a manner similar to that for the electrochemical tests, removing Nafion to prevent undesired interference. The hXAS experiments were performed at Beam Line 4-1, both Ni and Fe K-edge spectra were collected in fluorescence mode with the samples aligned at an angle of ~45° with respect to the incident beam and the Lytle detector. To minimize the background from elastic and Compton scattering, Z−1 filters (for example, a Mn filter for the Fe K-edge and a Co filter for the Ni K-edge) with Soller slits were placed before the window of the detector. Pure metal foils were used to align the threshold energy E_0 to 7,113 and 8,333 eV for Fe and Ni, respectively. A custom-designed cell was used to perform the operando measurements. Specifically, a cuvette was used as the main cell, and on one side, a circular hole with the diameter of 5 mm was cut, with the centre of the hole ~10 mm higher than the bottom of the cuvette. Then, a 1-µm-thick silicon nitride window (5 × 5 mm on a 10 × 10 mm, 200-µm-thick silicon supporting frame), with a Cr adhesion layer (5 nm) and a Au layer (20 nm), was used as the working electrode. The ink was prepared with water as the solvent and then added dropwise onto the electrode with a mass loading of 0.15 mg cm^{-2}. A silver wire was connected to the Au layer with silver paste to conduct electrons, and then the whole electrode was attached to the cuvette with Fe-free epoxy to keep the window just above the hole touching the electrolyte (1 M KOH) inside. During operando XAS measurements, a three-electrode set-up using a Pt counter electrode (DOE Business Centre for Precious Metals Sales and Recovery) and an Ag/AgCl/saturated-KCl reference electrode (ET072, CH Instruments)

was controlled using a potentiostat (SP-300, BioLogic). The EXAFS data were averaged and normalized using SIXPack and spline-fitted using IFEFFIT39 through the Athena graphical user interface[62–64].

Soft XAS for Ni, Fe L-edge and O K-edge was performed at Beam Line 10-1. Samples for soft XAS were mounted on a ¾ inch aluminium stick at an angle of about 55° with respect to the incident beam. A 1,000-lines-per-mm spherical grating monochromator with 20 µm entrance and exit slits was applied to provide ~10^{11} photons per s at 0.2 eV resolution in a 1 mm^2 beam spot. Spectra were acquired using a silicon photodiode (AXUV100) for total fluorescence yield mode and a Scienta SES-100 analyser for total electron yield mode.

Synchrotron HERFD-XAS measurements

The HERFD-XAS measurements were carried out at the 2-ID-D beamline of Advanced Photon Source, Argonne National Laboratory. The measurements were performed at the interfacial area about 8 µm from the electrode surface. The spectra were collected with a step size of 0.5 eV covering an energy range of 60 eV. The fluorescent X-rays were detected using a single-element Vortex silicon drift detector. A schematic of the experimental set-up can be found in ref. 48. The raw data were processed and quantified using XPS-MAPS[61].

DFT computational details

All periodic DFT calculations with spin polarization were performed using Vienna ab initio simulation package (VASP)[65]. Core and valence electrons were described using the projector-augmented wave pseudopotentials with the cut-off energy of 400 eV. Exchange–correlation was treated at the generalized gradient approximation level using the Perdew–Burke–Ernzerhof (PBE) functional, and the Gaussian smearing method was chosen with a width of 0.05 eV. The precision was set to 'accurate'. To account for on-site Coulomb repulsion in the strongly correlated 3*d* orbitals of Ni and Fe, the rotationally invariant DFT+U method was adopted with effective Hubbard parameters (U_{eff}) of 6.2 and 3.5 eV, respectively. The van der Waals interactions were included with Grimme's DFT-D3 scheme. Implicit solvation was used through both the VASPsol[66] and VASPsol++[67] packages with a continuum dielectric description of the electrolytes. To describe the experimental aqueous solution (1 M KOH) in VASPsol, the dielectric constant was set to 78.4, and a Debye screening length of 3 Å was used. To represent the experimental aqueous solution (1 M KOH) in VASPsol++[67], the concentration of the electrolyte, ionic radius and ion valency were set as 1 mol l^{-1}, 1.33 Å and 1.0, respectively. More detailed benchmarking shows that the ionic radius has a negligible effect on the adsorption energy calculations. For structure optimizations, the convergence criteria of energies and forces were set to 10^{-5} eV and 0.03 eV $Å^{-1}$, respectively.

Pure γ-NiOOH, Fe-doped γ-NiOOH, γ-$Fe_{0.25}Ni_{0.75}OOH$ and γ-FeOOH were constructed to investigate the OER active sites on the electrode, consistent with previous work by Friebel et al.[42]. As exported from the work of Friebel et al.[42], the unit cells for γ-NiOOH, γ-$Fe_{0.25}Ni_{0.75}OOH$ and γ-FeOOH were further optimized in this study. As the $(01\bar{1}2)$ surface has undercoordinated metal sites, it was found to have a high OER activity and thus was chosen as the termination facet of γ-NiOOH and γ-$Fe_{0.25}Ni_{0.75}OOH$ (Supplementary Fig. 33). The $(01\bar{1}2)$ surface was constructed with three surface unit meshes in the *x* direction and four metal sites in each surface unit mesh, and four O–metal–O layers in the *z* direction. The undercoordinated oxygens exposed on the surface were saturated with hydrogens, which were found to be thermodynamically stable under moderate OER conditions. In the slab models, two bottom O–metal–O layers are fixed in their bulk positions. To avoid spurious interactions between periodic slabs, a 30 Å vacuum gap was used. Finally, the surface models were constructed, representing the structure of the NiO_xH_y and $FeNiO_xH_y$ catalysts (Supplementary Fig. 33). Both Fe-doped γ-NiOOH and γ-$Fe_{0.25}Ni_{0.75}OOH$ have been widely adopted to represent MNF hydroxide catalysts (Supplementary Fig. 33), and both of these were included in this study. For γ-FeOOH, we used the (001) surface, consistent with ref. 42. The Brillouin zones for the unit cell and the slab were sampled using Monkhorst–Pack meshes of $6 \times 6 \times 2$ and $1 \times 1 \times 1$, respectively.

Thermodynamics under constant potential using GC-DFT

The constant-potential method within VASPsol++ was recently developed by Islam et al.[67] utilizing a nonlinear, nonlocal implicit model within the framework of GC-DFT. In this method, the Fermi level of the electrode is referenced to the bulk electrolyte and can be controlled by tuning the number of electrons in the system. In addition to the high accuracy of the new electrolyte model, this approach has been successfully integrated into VASP, significantly enhancing the efficiency of GC-DFT by enabling all calculations to be performed within VASP itself. As a result, the constant-potential method becomes computationally tractable for large, complex systems, as demonstrated in this study.

Although GC-DFT based on the VASPsol[66] and atomic simulation environment (ASE) interfaces[68] has been widely applied in numerous scientific studies, it suffers from slow input/output of charge density, wavefunction and local potential files, significantly limiting its applicability to large and complex systems. To overcome this challenge, GC-DFT at 1.53 V vs RHE using VASPsol++ was used here to model large systems comprising ~200 atoms, ensuring both computational efficiency and accuracy.

When performing constant-potential calculations, the grand-canonical energy of the system (Ω_{tot}) with only implicit solvation is calculated as:

$$\Omega_{tot} = A_{tot} - \mu_{e^-} \times N_{e^-} \quad (2)$$

where A_{tot} is the energy of the system within the implicit solvation at 1.53 V vs RHE, μ_{e^-} is the chemical potential of an electron and N_{e^-} is the number of electrons added to (positive in sign) or removed from (negative in sign) the neural systems.

In contrast to systems with only implict solvation, the grand-canonical energy of the system with hybrid solvation (Ω_{sys}) is determined by:

$$\Omega_{sys} = \Omega_{tot} - n_{H_2O}A_{H_2O} - n_{HB}E_{HBcorr} \quad (3)$$

where n_{H_2O} is the number of explicit H_2O molecules, A_{H_2O} is the energy of implicitly solvated H_2O molecules, n_{HB} is the total number of hydrogen bonds involving explicit waters, and E_{HBcorr} denotes the correction applied to each hydrogen bond (−0.18 eV), which has been benchmarked using the PBE functional to reproduce the self-solvation energy of water in the process $H_2O(g) + 4H_2O \rightarrow H_2O{\cdot}4H_2O$. In Fig. 4b, $n_{HB} = 6$. More details regarding the hydrogen-bond correction can be found in ref. 67.

The Gibbs free energy (*G*) was calculated as:

$$G = \Omega_{tot} + E_{ZPE} + C_pT - TS \quad (4)$$

in which E_{ZPE}, C_p and *S* are the zero-point energy, the heat capacity and the entropy of each gas-phase species or surface intermediate, respectively, and *T* is the thermodynamic temperature. The E_{ZPE}, C_p and *S* values of the surface intermediates were calculated within the harmonic approximation. The ASE package was used to calculate the Gibbs free energy of gaseous and adsorbed species at 298 K and 1 atm. The free energy of liquid water is calculated using the vapour pressure of gas-phase water at 298 K (0.035 bar). The thermodynamic terms and corrections for gas-phase molecules and surface adsorbates are provided in Supplementary Table 1.

Computational hydrogen electrode under alkaline conditions

The computational hydrogen electrode was used to calculate the free energy changes of elementary steps in our system. The hydrogen

evolution reaction in alkaline aqueous solution (pH = 14) and its standard electrode potential (U^0, versus the standard hydrogen electrode (SHE)) are shown below:

$$H_2O(l) + e^- \leftrightarrow \frac{1}{2}H_2(g) + OH^-(aq) \quad U^0 = -0.83\,V \text{ vs SHE} \tag{5}$$

where μ_i denotes the chemical potential of species i and e is the elementary charge.

The chemical potential of the hydroxyl–electron pair can be expressed on the RHE scale as follows:

$$\mu_{OH^-} - \mu_{e^-} = -\frac{1}{2}\mu_{H_2} + \mu_{H_2O} + eU_{RHE} \tag{6}$$

$$U_{RHE} = 0.0592 \times pH + U_{SHE} \tag{7}$$

Data availability

Source data are provided with this paper. The atomic coordinates of the optimized computational models are also provided. Other data that support the findings of this study are available from the corresponding authors upon reasonable request.

References

1. Nørskov, J. K., Bligaard, T., Rossmeisl, J. & Christensen, C. H. Towards the computational design of solid catalysts. *Nat. Chem.* **1**, 37–46 (2009).
2. Thorarinsdottir, A. E., Veroneau, S. S. & Nocera, D. G. Self-healing oxygen evolution catalysts. *Nat. Commun.* **13**, 1243 (2022).
3. Nong, H. N. et al. Key role of chemistry versus bias in electrocatalytic oxygen evolution. *Nature* **587**, 408–413 (2020).
4. Gorlin, M. et al. Oxygen evolution reaction dynamics, Faradaic charge efficiency, and the active metal redox states of Ni–Fe oxide water splitting electrocatalysts. *J. Am. Chem. Soc.* **138**, 5603–5614 (2016).
5. Grimaud, A. et al. Activating lattice oxygen redox reactions in metal oxides to catalyse oxygen evolution. *Nat. Chem.* **9**, 457–465 (2017).
6. Zou, S. et al. Fe (oxy)hydroxide oxygen evolution reaction electrocatalysis: intrinsic activity and the roles of electrical conductivity, substrate, and dissolution. *Chem. Mater.* **27**, 8011–8020 (2015).
7. Guo, J. et al. Direct seawater electrolysis by adjusting the local reaction environment of a catalyst. *Nat. Energy* **8**, 264–272 (2023).
8. Wang, X. et al. Pivotal role of reversible NiO_6 geometric conversion in oxygen evolution. *Nature* **611**, 702–708 (2022).
9. Yang, H. et al. Intramolecular hydroxyl nucleophilic attack pathway by a polymeric water oxidation catalyst with single cobalt sites. *Nat. Catal.* **5**, 414–429 (2022).
10. Righi, G. et al. On the origin of multihole oxygen evolution in haematite photoanodes. *Nat. Catal.* **5**, 888–899 (2022).
11. Bai, L., Hsu, C.-S., Alexander, D. T. L., Chen, H. M. & Hu, X. Double-atom catalysts as a molecular platform for heterogeneous oxygen evolution electrocatalysis. *Nat. Energy* **6**, 1054–1066 (2021).
12. Li, J. et al. Reaction kinetics and interplay of two different surface states on hematite photoanodes for water oxidation. *Nat. Commun.* **12**, 255 (2021).
13. Zhang, W. & Cao, R. Switching the O–O bond-formation mechanism by controlling water activity. *Chem* **7**, 1981–1982 (2021).
14. Roy, C. et al. Impact of nanoparticle size and lattice oxygen on water oxidation on $NiFeO_xH_y$. *Nat. Catal.* **1**, 820–829 (2018).
15. Dickens, C. F., Kirk, C. & Nørskov, J. K. Insights into the electrochemical oxygen evolution reaction with ab initio calculations and microkinetic modeling: beyond the limiting potential volcano. *J. Phys. Chem. C* **123**, 18960–18977 (2019).
16. Montoya, J. H. et al. Materials for solar fuels and chemicals. *Nat. Mater.* **16**, 70–81 (2017).
17. Kondo, M., Tatewaki, H. & Masaoka, S. Design of molecular water oxidation catalysts with earth-abundant metal ions. *Chem. Soc. Rev.* **50**, 6790–6831 (2021).
18. Seh, Z. W. et al. Combining theory and experiment in electrocatalysis: insights into materials design. *Science* **355**, eaad4998 (2017).
19. Velasco-Vélez, J.-J. et al. Surface electron–hole rich species active in the electrocatalytic water oxidation. *J. Am. Chem. Soc.* **143**, 12524–12534 (2021).
20. Craig, M. J. et al. Universal scaling relations for the rational design of molecular water oxidation catalysts with near-zero overpotential. *Nat. Commun.* **10**, 4993 (2019).
21. Wang, N. et al. Doping shortens the metal/metal distance and promotes OH coverage in non-noble acidic oxygen evolution reaction catalysts. *J. Am. Chem. Soc.* **145**, 7829–7836 (2023).
22. Zhang, N. & Chai, Y. Lattice oxygen redox chemistry in solid-state electrocatalysts for water oxidation. *Energy Environ. Sci.* **14**, 4647–4671 (2021).
23. Hong, W. T. et al. Charge-transfer-energy-dependent oxygen evolution reaction mechanisms for perovskite oxides. *Energy Environ. Sci.* **10**, 2190–2200 (2017).
24. Chen, F.-Y., Wu, Z.-Y., Adler, Z. & Wang, H. Stability challenges of electrocatalytic oxygen evolution reaction: from mechanistic understanding to reactor design. *Joule* **5**, 1704–1731 (2021).
25. Samira, S. et al. Dynamic surface reconstruction unifies the electrocatalytic oxygen evolution performance of nonstoichiometric mixed metal oxides. *JACS Au* **1**, 2224–2241 (2021).
26. Wen, Y. et al. Stabilizing highly active Ru sites by suppressing lattice oxygen participation in acidic water oxidation. *J. Am. Chem. Soc.* **143**, 6482–6490 (2021).
27. Zhao, S. et al. Structural transformation of highly active metal–organic framework electrocatalysts during the oxygen evolution reaction. *Nat. Energy* **5**, 881–890 (2020).
28. Chung, D. Y. et al. Dynamic stability of active sites in hydr(oxy) oxides for the oxygen evolution reaction. *Nat. Energy* **5**, 222–230 (2020).
29. Kuai, C. et al. Phase segregation reversibility in mixed-metal hydroxide water oxidation catalysts. *Nat. Catal.* **3**, 743–753 (2020).
30. Kuai, C. et al. Revealing the dynamics and roles of iron incorporation in nickel hydroxide water oxidation catalysts. *J. Am. Chem. Soc.* **143**, 18519–18526 (2021).
31. Trotochaud, L., Young, S. L., Ranney, J. K. & Boettcher, S. W. Nickel–iron oxyhydroxide oxygen-evolution electrocatalysts: the role of intentional and incidental iron incorporation. *J. Am. Chem. Soc.* **136**, 6744–6753 (2014).
32. Corrigan, D. A. The catalysis of the oxygen evolution reaction by iron impurities in thin film nickel oxide electrodes. *J. Electrochem. Soc.* **134**, 377 (1987).
33. Klaus, S., Cai, Y., Louie, M. W., Trotochaud, L. & Bell, A. T. Effects of Fe electrolyte impurities on $Ni(OH)_2$/NiOOH structure and oxygen evolution activity. *J. Phys. Chem. C* **119**, 7243–7254 (2015).
34. Michael, J. D. et al. Alkaline electrolyte and Fe impurity effects on the performance and active-phase structure of NiOOH thin films for OER catalysis applications. *J. Phys. Chem. C* **119**, 11475–11481 (2015).
35. Stevens, M. B., Trang, C. D. M., Enman, L. J., Deng, J. & Boettcher, S. W. Reactive Fe-sites in Ni/Fe (oxy)hydroxide are responsible for exceptional oxygen electrocatalysis activity. *J. Am. Chem. Soc.* **139**, 11361–11364 (2017).
36. Akbashev, A. R. et al. Probing the stability of $SrIrO_3$ during active water electrolysis via operando atomic force microscopy. *Energy Environ. Sci.* **16**, 513–522 (2023).

37. Bao, F. et al. Host, suppressor, and promoter—the roles of Ni and Fe on oxygen evolution reaction activity and stability of NiFe alloy thin films in alkaline media. *ACS Catal.* **11**, 10537–10552 (2021).
38. Hu, C. et al. Surface-enhanced Raman spectroscopic evidence of key intermediate species and role of NiFe dual-catalytic center in water oxidation. *Angew. Chem. Int. Ed.* **60**, 19774–19778 (2021).
39. Mefford, J. T. et al. Correlative operando microscopy of oxygen evolution electrocatalysts. *Nature* **593**, 67–73 (2021).
40. Peng, L. et al. Atomic cation-vacancy engineering of NiFe-layered double hydroxides for improved activity and stability towards the oxygen evolution reaction. *Angew. Chem. Int. Ed.* **60**, 24612–24619 (2021).
41. Chen, J. et al. Interfacial interaction between FeOOH and Ni–Fe LDH to modulate the local electronic structure for enhanced OER electrocatalysis. *ACS Catal.* **8**, 11342–11351 (2018).
42. Friebel, D. et al. Identification of highly active Fe sites in (Ni,Fe) OOH for electrocatalytic water splitting. *J. Am. Chem. Soc.* **137**, 1305–1313 (2015).
43. Hausmann, J. N. & Menezes, P. W. Effect of surface-adsorbed and intercalated (oxy)anions on the oxygen evolution reaction. *Angew. Chem. Int. Ed.* **61**, e202207279 (2022).
44. Li, N. et al. Influence of iron doping on tetravalent nickel content in catalytic oxygen evolving films. *Proc. Natl Acad. Sci. USA* **114**, 1486–1491 (2017).
45. Xiao, H., Shin, H. & Goddard, W. A. III Synergy between Fe and Ni in the optimal performance of (Ni,Fe)OOH catalysts for the oxygen evolution reaction. *Proc. Natl Acad. Sci. USA* **115**, 5872–5877 (2018).
46. Kuai, C. et al. Fully oxidized Ni–Fe layered double hydroxide with 100% exposed active sites for catalyzing oxygen evolution reaction. *ACS Catal.* **9**, 6027–6032 (2019).
47. Hu, A. et al. Manipulating interfacial dissolution–redeposition dynamics to resynthesize electrode surface chemistry. *ACS Energy Lett.* **7**, 2588–2594 (2022).
48. Zhang, Y., Hu, A., Maxey, E., Li, L. & Lin, F. Spatiotemporal visualization and chemical identification of the metal diffusion layer at the electrochemical interface. *J. Electrochem. Soc.* **169**, 100512 (2022).
49. Hu, A. et al. Uncovering phase transformation, morphological evolution, and nanoscale color heterogeneity in tungsten oxide electrochromic materials. *J. Mater. Chem. A* **8**, 20000–20010 (2020).
50. Zhang, Y. et al. Operando characterization and regulation of metal dissolution and redeposition dynamics near battery electrode surface. *Nat. Nanotechnol.* **18**, 790–797 (2023).
51. Feng, C., She, X., Xiao, Y. & Li, Y. Direct detection of Fe(VI) water oxidation intermediates in an aqueous solution. *Angew. Chem. Int. Ed.* **62**, e202218738 (2023).
52. Hunter, B. M. et al. Trapping an iron(VI) water-splitting intermediate in nonaqueous media. *Joule* **2**, 747–763 (2018).
53. Yu, X. & Licht, S. Advances in electrochemical Fe(VI) synthesis and analysis. *J. Appl. Electrochem.* **38**, 731–742 (2008).
54. Kemner, K. M. et al. XAS investigations of Fe(VI). *J. Synchrotron Radiat.* **8**, 949–951 (2001).
55. Saveleva, V. A. et al. Operando evidence for a universal oxygen evolution mechanism on thermal and electrochemical iridium oxides. *J. Phys. Chem. Lett.* **9**, 3154–3160 (2018).
56. Drevon, D. et al. Uncovering the role of oxygen in Ni-Fe(O_xH_y) electrocatalysts using in situ soft X-ray absorption spectroscopy during the oxygen evolution reaction. *Sci. Rep.* **9**, 1532 (2019).
57. Reith, L. et al. In situ detection of iron in oxidation states ≥ IV in cobalt-iron oxyhydroxide reconstructed during oxygen evolution reaction. *Adv. Energy Mater.* **13**, 2203886 (2023).
58. Lee, S., Bai, L. & Hu, X. Deciphering iron-dependent activity in oxygen evolution catalyzed by nickel-iron layered double hydroxide. *Angew. Chem. Int. Ed.* **59**, 8072–8077 (2020).
59. Lee, S., Banjac, K., Lingenfelder, M. & Hu, X. Oxygen isotope labeling experiments reveal different reaction sites for the oxygen evolution reaction on nickel and nickel iron oxides. *Angew. Chem. Int. Ed.* **58**, 10295–10299 (2019).
60. Medford, A. J. et al. Assessing the reliability of calculated catalytic ammonia synthesis rates. *Science* **345**, 197–200 (2014).
61. Glowacki, A. T. XRF-MAPS (US Department of Energy, 2020)
62. Webb, S. M. SIXPack a graphical user interface for XAS analysis using IFEFFIT. *Phys. Scripta* **T115**, 1011–1014 (2005).
63. Newville, M. IFEFFIT: interactive XAFS analysis and FEFF fitting. *J. Synchrotron Rad.* **8**, 322–324 (2001).
64. Ravel, B. & Newville, M. ATHENA, ARTEMIS, HEPHAESTUS: data analysis for X-ray absorption spectroscopy using IFEFFIT. *J. Synchrotron Rad.* **12**, 537–541 (2005).
65. Kresse, G. & Furthmüller, J. Efficient iterative schemes for ab initio total-energy calculations using a plane-wave basis set. *Phys. Rev. B Condens. Matter.* **54**, 11169–11186 (1996).
66. Mathew, K., Kolluru, V. S. C., Mula, S., Steinmann, S. N. & Hennig, R. G. Implicit self-consistent electrolyte model in plane-wave density-functional theory. *J. Chem. Phys.* **151**, 234101 (2019).
67. Islam, S. M. R., Khezeli, F., Ringe, S. & Plaisance, C. An implicit electrolyte model for plane wave density functional theory exhibiting nonlinear response and a nonlocal cavity definition. *J. Chem. Phys.* **159**, 234117 (2023).
68. Larsen, A. H. et al. The atomic simulation environment—a Python library for working with atoms. *J. Phys. Condens. Matter.* **29**, 273002 (2017).

Acknowledgements

The work at Virginia Tech was supported by Department of Chemistry start-up funds and the Institute for Critical Technology and Applied Science (F.L.). F.L. also acknowledges the seedling support from the Virginia Tech College of Science Strategic Initiative in Energy (03400) and the support from the Leo and Melva Harris Faculty Fellowship. L. Liu and H.X. gratefully acknowledge the financial support from the National Science Foundation Chemical Catalysis program (CHE-2102363) (H.X.) and the computational resource provided by Advanced Research Computing at Virginia Tech. This research used resources of the Advanced Photon Source, a US Department of Energy (DOE) Office of Science User Facility operated for the DOE Office of Science by Argonne National Laboratory under contract no. DE-AC02-06CH11357. Use of the Stanford Synchrotron Radiation Lightsource, SLAC National Accelerator Laboratory, is supported by the US Department of Energy, Office of Science, Office of Basic Energy Sciences under contract no. DE-AC02-76SF00515.

Author contributions

F.L. and C.K. conceived the project. C.K. and F.L. designed the overall experiments. C.K., F.L. and L. Li developed the fluorescence imaging measurements. L. Liu and H.X. conducted the DFT calculations and microkinetic analysis. C.K. synthesized the materials and performed the characterization and electrochemical measurements. C.K. and Yan Zhang performed the soft-XAS and operando hXAS experiments with assistance from D.N. and D.S. The synchrotron XFM and HERFD experiments were performed by A.H., Yuxin Zhang and D.X. under the supervision of F.L. and L. Li. The hXAS measurements for key reference samples were performed by D.D. and G.D. The figures were prepared by C.K., L. Liu, H.X. and F.L., who also wrote the manuscript with assistance from all co-authors. All of the co-authors participated in the scientific discussion and approved the manuscript submission.

Competing interests

The authors declare no competing interests.

Additional information

Supplementary information The online version contains supplementary material available at https://doi.org/10.1038/s41929-025-01342-5.

Correspondence and requests for materials should be addressed to Chunguang Kuai, Hongliang Xin, Luxi Li or Feng Lin.

Peer review information *Nature Catalysis* thanks the anonymous reviewer(s) for their contribution to the peer review of this work.